PHILOSOPHICAL MAGAZINE A, 1998, VOL. 77, NO. 3, 801–823

Observations and modelling of $a\langle 011\rangle$ dislocations in NiAl at intermediate temperatures

BY M. J. MILLS, R. SRINIVASAN

Department of Materials Science and Engineering, The Ohio State University, Columbus, Ohio 43210, USA

and M. S. DAW

Department of Physics and Astronomy, Clemson University, Clemson, South Carolina 29634-1911, USA

[*Received 5 July 1996 and accepted in revised form 16 July 1997*]

ABSTRACT

Recent experimental evidence indicates that dislocations of the type $a\langle 011\rangle$ are prominent in microstructures following deformation in hard-oriented NiAl at intermediate temperatures (above the brittle-to-ductile transition temperature). The structure of $a\langle 011\rangle$ dislocations has been examined using diffraction-contrast transmission electron microscopy. Evidence has been found for the decomposition of $a\langle 011\rangle$ dislocations into two $a\langle 001\rangle$ dislocations. Analysis using both anisotropic elasticity and the embedded-atom method calculations has revealed that this decomposition process is energetically favourable, even though the net core energy increases upon decomposition. Based on microstructural evidence, additional decomposition occurs by a combination of climb and glide. A continuum-based dislocation model is introduced which incorporates these relevant microstructural features. The predictions of this model are compared with characteristics of deformation of NiAl in the hard orientation.

§ 1. INTRODUCTION

The compound NiAl is an important intermetallic system of considerable technological interest. The attractive properties of NiAl (with the B2 structure) include a high melting point, relatively low density and excellent oxidation and corrosion resistances. Alloys based on NiAl are actively being studied as potential competitors to superalloys for aerospace turbine applications. In spite of the potential technological impact of NiAl and NiAl-based alloys, the useful range of application of these materials is limited by their tendency towards brittleness at lower temperatures and rapid loss of strength at higher temperatures.

There is substantial experimental evidence indicating that intricate details of dislocation behaviour play a central role in determining the deformation behaviour of NiAl at both low and high temperatures. For all crystal orientations other than $\langle 001\rangle$, the yield strength declines in a relatively monotonic fashion with temperature. Deformation by $a\langle 100\rangle$ dislocations is reported to dominate for the entire temperature regime (Wasilewski *et al.* 1967, Pascoe and Newey 1968). Remarkably different behaviour is observed for single crystals oriented along the $\langle 001\rangle$ or 'hard' orientation, for which no shear stress exists for glide of the preferred $a\langle 100\rangle$ dislocations. Yield strengths are generally much higher, and the variation in yield strength with temperature is no longer monotonic. At lower temperatures, the yield strength is

initially very high (approximately 2 GPa) and declines to a plateau value of about 1.4 GPa (Pascoe and Newey 1968). These very high yield strengths contribute to the brittleness of hard-oriented crystals in this temperature regime. In compression, these crystals deform either by motion of $a\langle 111\rangle$ dislocations (Pascoe and Newey 1968, Loretto and Wasilewski 1971, Kim 1990) or by kinking (Fraser *et al.* 1973a). Between room temperature and about 600 K in stoichiometric NiAl, the yield strength is relatively constant but then exhibits a dramatic decrease at higher temperatures. Although still the subject of intense debate in the literature, there is general agreement that the abrupt change in the temperature dependence of yielding corresponds to a transition from $a\langle 111\rangle$ dislocation activity at lower temperatures to non-$\langle 111\rangle$ activity at higher temperatures (Miracle 1993). Additional evidence indicating a change in deformation mechanism includes the relatively sudden increase in ductility and strain-rate sensitivity at higher temperatures (Lahrman *et al.* 1991). In early work, it was suggested that climb of $a\langle 010\rangle$ dislocations was principally responsible for deformation in this regime (Ball and Smallman 1966, Fraser *et al.* 1973b). However, since the homologous temperature is still rather low at this 'transition' temperature, it is unlikely that long-range climb of $a\langle 010\rangle$ dislocations could be entirely responsible for deformation at conventional values of strain rate (Miracle 1990). Alternatively, several recent studies have shown that $a\langle 011\rangle$ dislocations are important to the deformation of hard-oriented NiAl at intermediate temperatures (i.e. above the ductile-to-brittle transition temperature (DBTT)) (Kim 1990, Kim and Gibala 1991, Field *et al.* 1991). A similar slip transition has been reported for hard-oriented CoTi as well (Yoshida and Takasugi 1991). Therefore it has been suggested that the apparent change in deformation mechanism above the DBTT may be related to the onset of $a\langle 011\rangle$ dislocation activity.

Evidence indicating that glide motion of $a\langle 011\rangle$ dislocations may not be a simple process has been offered by recent high-resolution transmission electron microscopy (HRTEM) studies of the cores of $a\langle 011\rangle$ dislocations (Mills and Miracle 1993, Mills *et al.* 1993, 1995a). These studies have indicated that $a\langle 011\rangle$ dislocations are not in planar configurations but are in fact decomposed such that the Burgers vector content of the dislocation is actually split *out of the glide plane* of the total $a\langle 011\rangle$ dislocation. While these observations suggest that conventional glide motion of the $a\langle 011\rangle$ dislocation will be difficult, if not impossible, no attempt to incorporate these results into a model for the motion of these dislocations was attempted. In addition, the dislocation configurations for orientations other than pure edge were not investigated, and the importance of these other line orientations for describing flow was not considered.

In this paper, we report additional experimental results concerning the nature of this decomposition process based on transmission electron microscopy (TEM) examination of the structure and morphology of $a\langle 011\rangle$ dislocations. These observations have been conducted using NiAl bicrystals, based on previous work by Miracle (1991). Atomistic calculations using the embedded-atom method (EAM) (Daw and Baskes 1984) have also been conducted to explore the core structure of these dislocations under both static and dynamic conditions. Emerging from this work is evidence that the edge portions of $a\langle 011\rangle$ dislocations readily decompose into two $a\langle 010\rangle$ dislocations. Under the premise that these edge components are very difficult to move by glide, a dislocation-based model is introduced which considers instead that dislocation motion proceeds by the lateral motion of mixed and screw segments. It is proposed that the glide motion of these non-edge segments is constrained by a

diffusion-controlled process. The implications of this model in terms of the macroscopic flow behaviour are also described.

§ 2. Experimental and computational techniques

The dislocation microstructure produced by deformation of oriented bicrystals of stoichiometric NiAl was studied in this investigation. As described in detail elsewhere (Miracle 1990, 1991), this geometry was intended to promote the activation of non-$\langle 010\rangle$ slip in one of the crystals through both elastic and plastic incompatibilities, while maintaining a 'hard' overall orientation. Based on a previous investigation (Miracle 1990, 1991), a high density of $a\langle 011\rangle$ dislocations is produced in the hard-oriented crystal near the bicrystal boundary. This region of the sample was therefore ideal for the detailed analysis of the structure of $a\langle 011\rangle$ dislocations undertaken in this work. Slip on two orthogonal slip systems, $a[01\bar{1}]$ on (011) and $a[011]$ on (011) was found by slip trace analysis. Thin foils for TEM investigation were prepared by slicing the hard-oriented crystal parallel to the (011) slip plane for the $a[01\bar{1}]$ dislocations. TEM observations were conducted using a Phillips CM 200 operating at 200 kV.

Anisotropic elasticity calculations of relevant dislocation configurations have been performed using the elastic constants for stoichiometric NiAl (Rusovic and Warlimont 1977). The EAM calculations (Daw and Baskes 1984) were performed utilizing potentials developed specifically for NiAl (Rao *et al.* 1991). The static calculations were conducted by first establishing the atomic positions around the cores of the dislocations assuming anisotropic elasticity. The typical computational supercell was a cylinder with a 10 nm radius. The atoms in an outer ring of the supercell (1 nm thick) were held fixed during the relaxations to maintain the long-range elastic stress field around the dislocation. In order to compare the energies of core structures which might have different local compositions, the chemical potentials of Ni and Al were used, referenced to stoichiometric NiAl (see Foiles and Daw (1987) for an example of this procedure applied to Ni_3Al). In practice, this was accomplished by transforming the functions such that the energy for each Ni and Al atom in a perfect crystal was equal to their respective chemical potentials, without altering the physical content of the functions. This procedure is described in more detail in the appendix. Molecular dynamics calculations were also conducted to explore the effect of both stress and temperature on the core structures. Pure shear strains were imposed on the supercell; then the atoms in the outer ring of the supercell were held fixed. The imposed strain state was chosen in order to create maximum shear stresses for the $a[01\bar{1}]$ dislocation on the (011) slip plane, while no shear stresses were present for the $a[010]$ (001) or $a[00\bar{1}]$ (010) slip systems.

§ 3. Summary of transmission electron microscopy observations

Analysis of the overall dislocation microstructure in the hard-oriented crystal of the bicrystal specimen can be found elsewhere (Mills and Miracle 1993, Mills *et al.* 1993, 1995a, b). An example of the observed dislocation morphology can be seen in fig. 1, in which nearly all the dislocations in the field of view have Burgers vectors parallel to $[01\bar{1}]$. Macroscopic (011) slip traces are observed, which correspond to the glide plane for these dislocations. The plane of the TEM foil observed in fig. 1 is also (011). The shape of the dislocations suggest the expansion of dislocation loops from sources. A prominent feature of the loops is that they preferentially elongate in the

Fig. 1

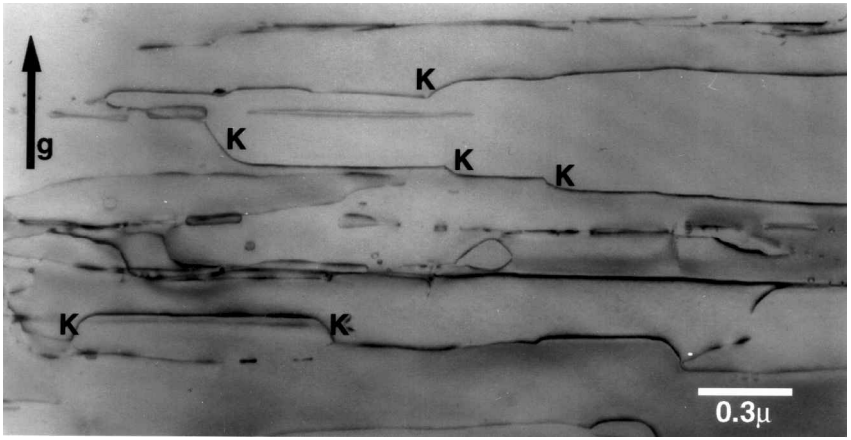

Bright-field TEM image of $a\langle 011\rangle$ dislocations. Long dislocations have Burgers vectors parallel to $\mathbf{g} = [0\bar{1}1]$. The beam direction (and foil plane normal) is $[011]$. Slip plane for these dislocations is (011). Dislocations are elongated in edge orientation. Kink-like features along near-edge portions of dislocations are labelled K.

edge orientation. This preferred orientation cannot be explained on the basis of line energy considerations since the edge orientation has 43% larger line energy than does the screw orientation (Miracle 1991, Glatzel 1993). These considerations suggest that the edge orientation has a relatively low mobility when compared with the other dislocation characters. Note that the near-edge portions of the loops are composed of relatively straight segments separated by steps of mixed character (indicated as K in fig. 1), suggesting the possibility of a 'kink-like' mechanism for the propagation of the near-edge dislocations. This possibility will be developed further in § 5.

HRTEM observations have been performed previously (Mills and Miracle, Mills *et al.* 1993b, 1995a) in an attempt to determine whether the low apparent mobility of the edges is due to an intrinsic feature related to the cores of these dislocations. Indeed, the HRTEM analysis indicates that $a[0\bar{1}1]$ edge dislocations (aligned along the $[100]$ direction) can decompose into two $a\langle 010\rangle$ dislocations via the reaction

$$a[0\bar{1}1](011) = a[0\bar{1}0](001) + a[001](010). \quad (1)$$

This is a decomposition reaction (rather than a dissociation) since no fault is formed between the two perfect $a\langle 010\rangle$ dislocations. The important consequences of this decomposition are that the product $a\langle 010\rangle$ dislocations firstly do not have a common glide plane and secondly experience no applied shear stress for axial deformation in the hard orientation. As a result, conservative glide of the $\langle 011\rangle$ edge dislocation is not possible.

Decomposition occurs along significant lengths of near-edge $a\langle 011\rangle$ dislocations, as indicated by diffraction contrast observations (Mills *et al.* 1995a). These effects may be summarized with the aid of fig. 2 which shows several $a[011]$ dislocations observed with a beam direction of $[011]$ (which is also the foil plane normal). Consequently, the slip plane for the $a[011]$ dislocations is viewed 'edge on'. These images were obtained using a $\mathbf{g}$-$3\mathbf{g}$ condition (deviation parameter

Fig. 2

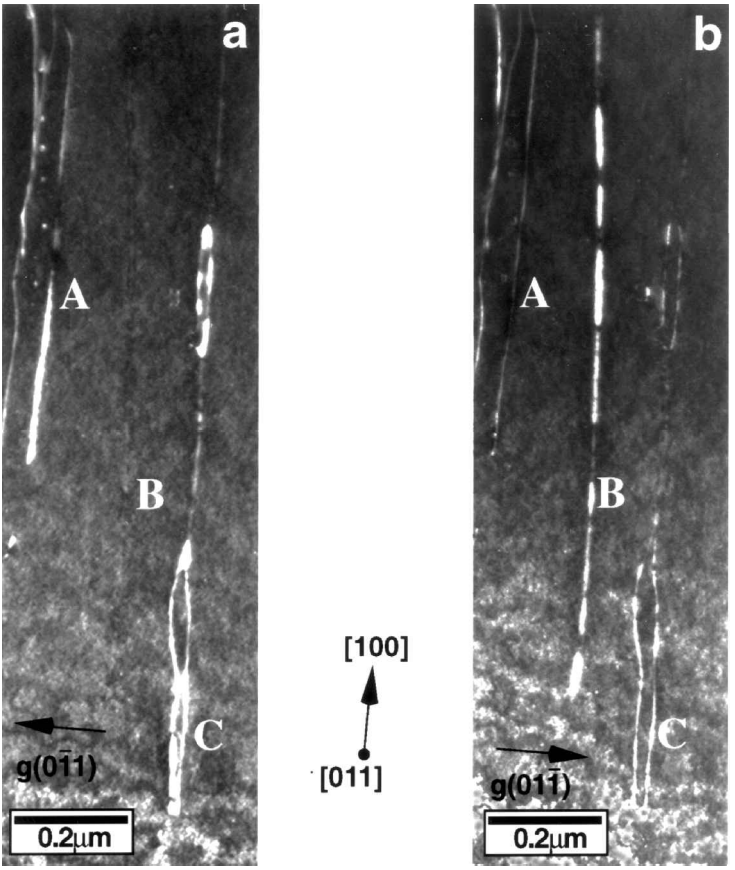

Dark-field TEM image of three $a[011]$ dislocations demonstrating the strong asymmetry in contrast which is observed upon changing the sign of the diffraction vector. (*a*) $\mathbf{g}$-$3\mathbf{g}$ image with $\mathbf{g} = [011]$ and (*b*) $\mathbf{g}$-$3\mathbf{g}$ image with $\mathbf{g} = [0\bar{1}1]$. Based on the analysis described in text, dislocations A and B have opposite Burgers vectors and are decomposed along significant lengths of their lines. Dislocation C has both compact and widely decomposed segments. Beam direction is parallel (or antiparallel) to the overall $[011]$ Burgers vector of these dislocations.

$s = 6 \times 10^{-3}$ Å^{-1}), where $\mathbf{g}$ is either of the diffraction vectors $[0\bar{1}1]$ and $[01\bar{1}]$, which should yield only weak residual contrast for a perfect $a[011]$ edge dislocation, since $\mathbf{g}\cdot\mathbf{b} = 0$ but $\mathbf{g}\cdot(\mathbf{b}\times\mathbf{u}) = 2$. Portions of the dislocation labelled A yield quite strong contrast for $\mathbf{g} = [0\bar{1}1]$ (fig. 2(*a*)), while very weak contrast is observed for the $\mathbf{g} = [01\bar{1}]$ diffraction vector (fig. 2(*b*)). A similar strong asymmetry of contrast is observed for the dislocation labelled B, although in this case strong contrast is observed for $\mathbf{g} = [01\bar{1}]$, while weak contrast is seen for $\mathbf{g} = [011]$. Multibeam image simulations (Mills *et al.* 1995a) indicate that this strong asymmetry of contrast (for positive and negative $\mathbf{g}$) is consistent with the fine-scale decomposition of the $a[011]$ dislocations via eqn. (1). This contrast arises since $\mathbf{g}\cdot\mathbf{b}_{001} = -\mathbf{g}\cdot\mathbf{b}_{010}$, creating a 'dipole-like' contrast effect. Additional simulations have indicated that strong contrast asymmetry will be present for

decomposition distances ranging between about 2 nm to about 20 nm. It is important to note that simulations for a perfect $a[0\bar{1}1]$ dislocation yield very weak residual contrast for *both* $\mathbf{g} = [0\bar{1}1]$ and $\mathbf{g} = [0\bar{1}\bar{1}]$ conditions (Mills *et al.* 1995a), so that the contrast asymmetry observed in fig. 2 clearly indicates decomposition of the $a[011]$ dislocation. This contrast asymmetry is commonly observed in the microstructures examined and appears to be most prominent along near-edge orientation for the $a[011]$ dislocations, indicating that the decomposition occurs preferentially along this orientation.

Another notable feature of fig. 2 which is commonly observed in the microstructures examined are segments such as that indicated as C, where a distinct flaring into two separate dislocation lines is apparent. The relative shift in the position of these two lines in this region for positive and negative **g** once again suggest a dipole contrast. The dark-field images in fig. 3 showing a similar segment demonstrate that such regions are in fact decomposed rather than dipole loops. In fig. 3(*a*), using a $\mathbf{g} = [\bar{1}01]$ reflection, dislocation $\mathbf{b}_2$ is out of contrast, while $\mathbf{b}_1$ is out of contrast using $\mathbf{g} = [\bar{1}\bar{1}0]$ as seen in fig. 3(*c*). Both of these segments are in contrast,

Fig. 3

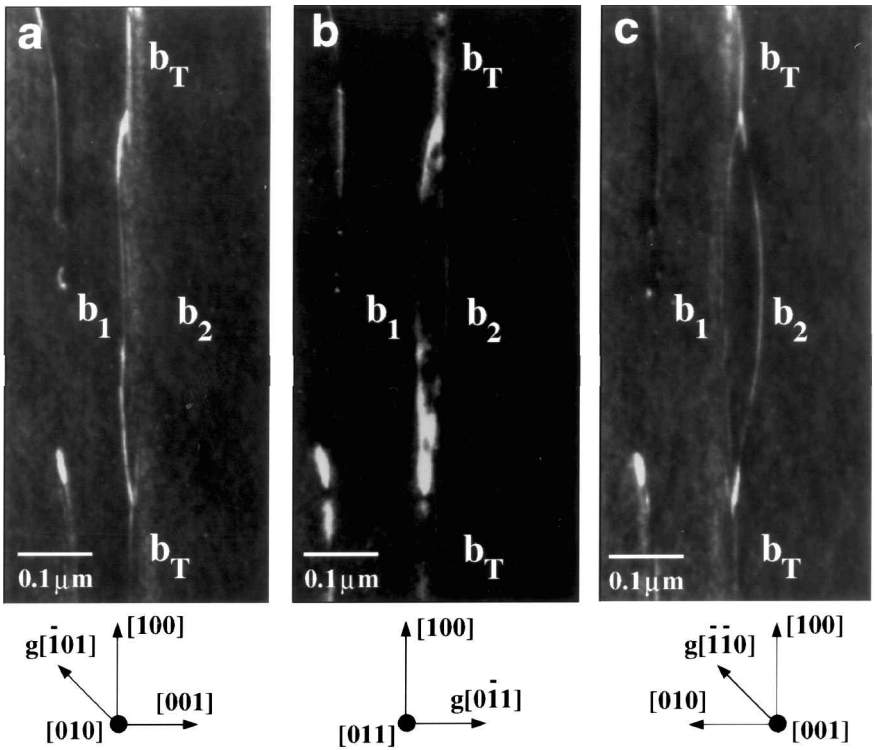

Dark-field image from a tilting experiment to determine nature of decomposition along one segment of the $a[011]$ dislocation shown in fig. 4. (*a*) [010] beam direction and $\mathbf{g} = [\bar{1}01]$. Note that dislocation $\mathbf{b}_1$ is in contrast. (*b*) [011] beam direction and $\mathbf{g} = [0\bar{1}1]$. Note that both dislocations $\mathbf{b}_1$ and $\mathbf{b}_2$ are in weak contrast. (*c*) [001] beam direction and $\mathbf{g} = [\bar{1}\bar{1}0]$. Note that dislocation $\mathbf{b}_2$ is in contrast. All images obtained for $\mathbf{g}$-3$\mathbf{g}$ conditions.

however, for $\mathbf{g} = [0\bar{1}1]$, seen in fig. 3(*b*). This set of images is consistent with the decomposition of $\mathbf{b}_T$ into the segments $\mathbf{b}_1 = a[001]$ and $\mathbf{b}_2 = a[010]$. The distance between the $a\langle 010\rangle$ dislocations is a maximum of about 70 nm in this case. Note that the 'dipole-like' asymmetry in contrast for the two diffraction conditions of figs. 2(*a*) and (*b*) is only observed in the widely decomposed segments, indicating that the other segments of the dislocation are relatively compact. These observations, combined with the diffraction contrast and previous HRTEM results, suggest that a wide range of decomposition distances may be present, even along the same dislocation.

A final important feature of these more widely decomposed segments is that the $a\langle 010\rangle$ dislocations evidently move by a combination of both climb and glide. This is indicated in the tilting experiments shown in fig. 4, in which a longer length of the same dislocation observed in fig. 3 is shown in two different orientations. In fig. 4(*a*), the dislocation is imaged near the [101] zone using $\mathbf{g} = [10\bar{1}]$ for which one of the dislocations in the decomposed segments ($\mathbf{b}_1 = a[001]$) is observed with its (010) glide plane viewed *edge on*. The segments $\mathbf{b}_1$ should be perfectly straight if they are contained entirely within their slip plane. However, in fact these segments are seen to have significant curvature, indicating that climb of the segment has occurred. The curved shape of segments $\mathbf{b}_2 = a[010]$ seen in fig. 4(*b*), which is imaged near the $[\bar{1}10]$ zone and using $\mathbf{g} = [110]$, indicates that it has also undergone climb motion. Both segments have also undergone some glide motion as indicated by the curved shapes of segments $\mathbf{b}_1$ in fig. 4(*b*) and segments $\mathbf{b}_2$ in fig. 4(*a*) (both seen in residual contrast). Taken together, these observations on the more widely decomposed segments such as these indicate that decomposition occurs through a combination of both glide and climb of the individual $a\langle 010\rangle$ dislocations.

The observation of extensive climb decomposition in these samples is somewhat surprising considering the relatively low homologous temperatures at which the bicrystal was tested ($T = 0{\cdot}36T_m$), suggesting that climb may occur by pipe diffusion, as is discussed in more detail below. Finally, these studies indicate that decomposition occurs primarily along the edge orientation of the $a\langle 011\rangle$ dislocations. The reason for this tendency is discussed in the next section, which describes the results of both continuum and atomistic calculations to explore the decomposition of the $a\langle 011\rangle$ dislocations.

§ 4. Continuum and atomistic calculations

We have studied the decomposition reaction $a[011](00\bar{1}) \rightarrow a[010](00\bar{1}) + a[001](010)$ by continuum elasticity theory and by atomistic calculations. For many dislocation reactions, the energy released by the elastic continuum dominates any 'core' energies and determines whether the reaction takes place. In the case studied here, the elastic energy prohibits the decomposition from occurring except precisely at edge orientation. At edge orientation, the 'core' energy not included in continuum theory is potentially important, and we complete the analysis by carrying out appropriate atomistic calculations. Our results verify that the decomposition should occur in the manner observed in the experiments. Preliminary results of these calculations have been reported previously (Mills *et al.* 1993, 1995a, b), but we analyse the results more completely in this paper.

Because the elastic strain energy of a dislocation, and the interaction between dislocations, diverges as the logarithm of the sample size, such energies tend to dominate over 'core' energies in most dislocation reactions. So we begin by

Fig. 4

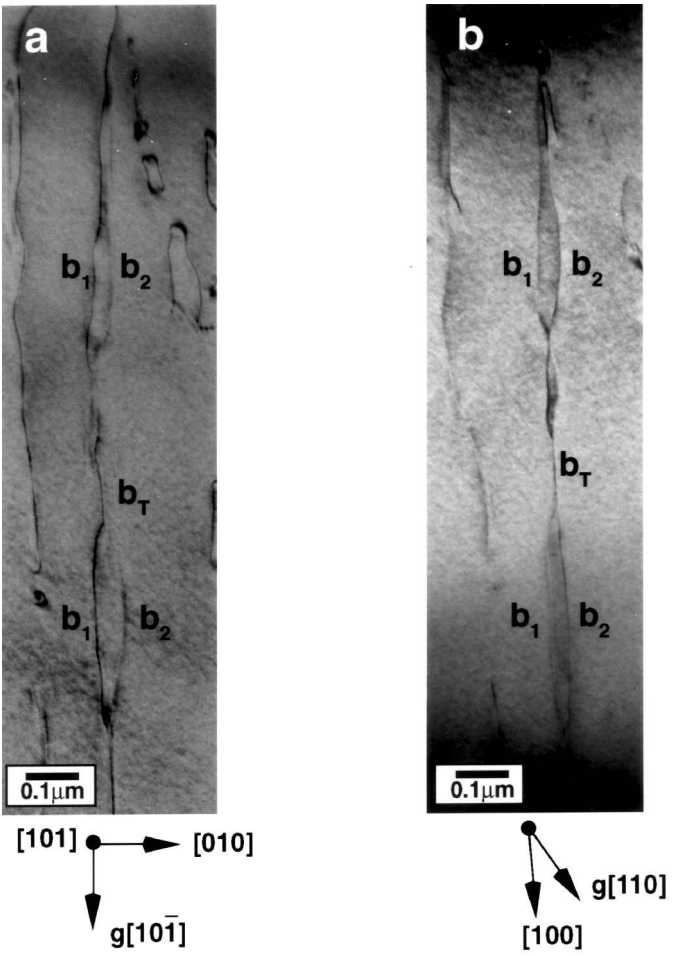

Bright-field image from a tilting experiment on dislocation shown in fig. 3. (*a*) Near $[\underline{1}01]$ zone using $\mathbf{g} = [\underline{1}01]$. Dislocation segments $\mathbf{b}_1$ (with Burgers vector $a[001]$) observed in strong contrast with glide plane edge-on. (*b*) Near $[\underline{1}10]$ zone, tilted 15° towards $[\underline{1}11]$ zone, and using $\mathbf{g} = [\underline{1}10]$. Dislocation segments $\mathbf{b}_2$ (the Burgers vector $a[010]$) observed in strong contrast with glide plane edge-on. Note that segments $\mathbf{b}_1$ in (*a*) and $\mathbf{b}_2$ in (*b*) are both clearly curved, indicating that decomposition involves significant climb motion.

examining the anisotropic elasticity theory of the two products. If the radial component of the force between the products is attractive, the reaction will be disallowed elastically. As shown in fig. 5, the radial force resists decomposition at all line directions except precisely at edge orientation, where the radial force vanishes. Consequently, it is expected that the edge line direction should be susceptible to decomposition. This conclusion would appear to be in accord with firstly the general shape of these dislocations as observed in fig. 1 and secondly the finding that direct evidence of decomposition in the diffraction contrast TEM images has only been obtained for dislocations near edge orientation.

Fig. 5

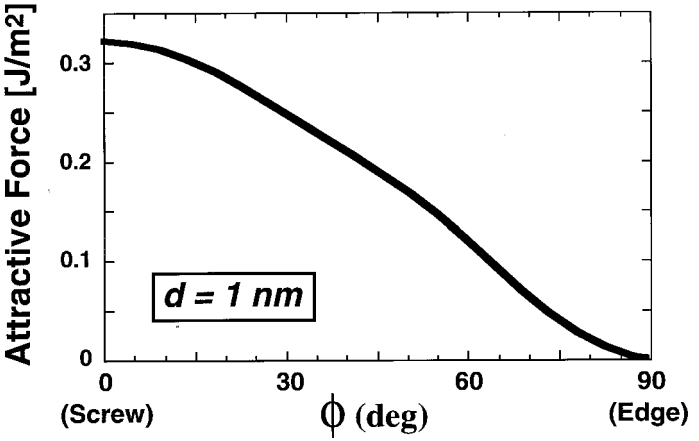

Anisotropic elasticity calculation of force of attraction between $a\langle 010\rangle$ dislocations in decomposed configuration as a function of character of overall $a[011]$ dislocation. $a\langle 010\rangle$ dislocations are assumed to decompose normal to (011) glide plane of overall $a[011]$ dislocation, with a separation of 1 nm.

Again, using anisotropic elasticity, we examined the decomposition when the perfect dislocation is aligned with the edge orientation. Figure 6 presents a plot of the vector forces acting on the $a[001]$ dislocation if it were positioned at various locations relative to the $a[010]$, which is assumed to be fixed at the origin of the plot. We see that the elastic forces push the decomposition products into stable alignment perpendicular to the (011) glide plane. This relative motion could occur by a combination of glide and climb. Note that there is no radial component to the elastic force, only an angular component.

Qualitatively the same behaviour is obtained in an isotropic medium. We examine the expressions here to illustrate the behaviour. For a dislocation of Burgers vector $\mathbf{b}_{\text{tot}}$ and line direction $\hat{\xi}$, the energy per unit length is (Hirth and Lothe 1982).

$$\frac{W_{\text{b}}}{L} = \frac{\mu}{4\pi}(\mathbf{b}_{\text{tot}} \cdot \mathbf{K} \cdot \mathbf{b}_{\text{tot}}) \ln\left(\frac{R}{r_0}\right), \tag{2}$$

where $\mathbf{K} = (1 - \upsilon)^{-1}(\mathbf{1} - \upsilon\hat{\xi}\hat{\xi})$, μ and υ are the shear modulus and Poisson's ratio respectively, and R and r_0 are the outer and inner cut-off radii respectively. If the dislocation splits into two dislocations with Burgers vectors $\mathbf{b}_1$ and $\mathbf{b}_2$, separated by $\hat{\mathbf{r}}$, then the energy per unit length is

$$\frac{W_{\text{a}}}{L} = \frac{\mu}{4\pi}(\mathbf{b}_1 \cdot \mathbf{K} \cdot \mathbf{b}_1 + \mathbf{b}_2 \cdot \mathbf{K} \cdot \mathbf{b}_2) \ln\left(\frac{R}{r_0}\right) + \frac{\mu}{2\pi}(\mathbf{b}_1 \cdot \mathbf{K} \cdot \mathbf{b}_2) \ln\left(\frac{R}{r}\right) - \frac{\mu}{2\pi(1 - \upsilon)}\left[(\mathbf{b}_1 \times \hat{\xi}) \cdot \hat{\mathbf{r}}\right]\left[(\mathbf{b}_2 \times \hat{\xi}) \cdot \hat{\mathbf{r}}\right]. \tag{3}$$

The first term is the self-energy of the two products. The last two terms are the interaction energy; the first depends only on distance and the second only on

Fig. 6

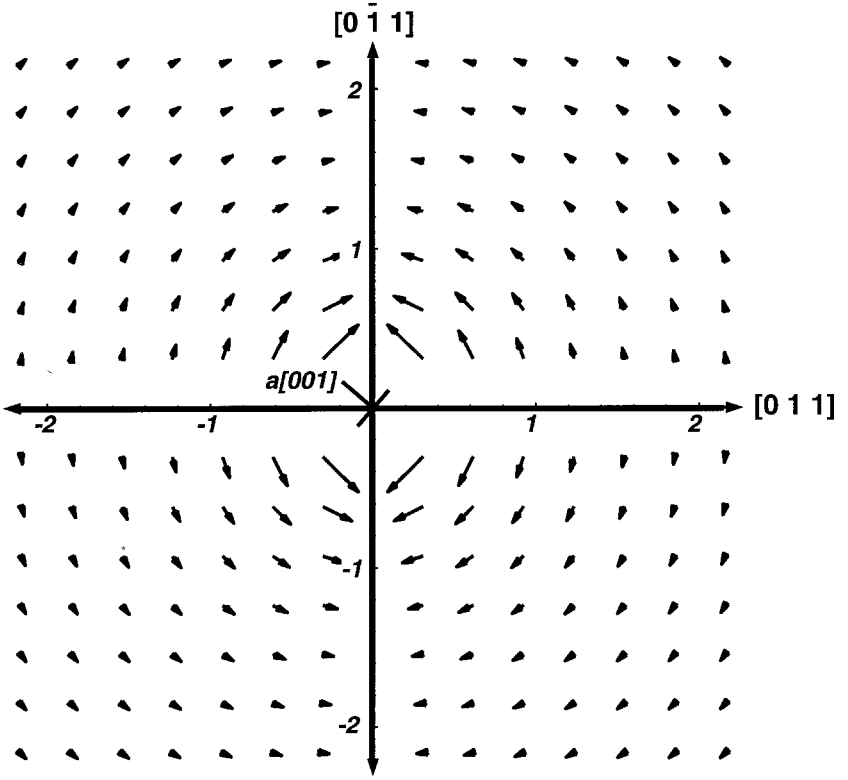

Vector plot showing the interaction forces acting on $a[010]$ dislocations due to the presence of an $a[001]$ dislocation fixed at the origin. The length of arrows indicates the magnitude of forces (arbitrary units). Note that forces are minimized for decomposition normal to be (011) glide plane of the total $a[011]$ dislocation.

angle. Note also that the last term is independent of R. The decomposition energy is then

$$\frac{\Delta W}{L} = -\frac{\mu}{2\pi}(\mathbf{b}_1 \cdot \mathbf{K} \cdot \mathbf{b}_2) \ln\left(\frac{r}{r_0}\right) - \frac{\mu}{2\pi(1-\upsilon)}\left[(\mathbf{b}_1 \times \hat{\xi}) \cdot \hat{\mathbf{r}}\right]\left[(\mathbf{b}_2 \times \hat{\xi}) \cdot \hat{\mathbf{r}}\right]. \quad (4)$$

The first term gives rise to a radial force which resists decomposition; this term vanishes for edge dislocations with mutually perpendicular Burgers vectors. The second term is independent of distance and depends only on the orientation of the products. If the products are oriented at an angle θ with respect to the slip direction, the second term varies as $\cos 2(\theta)$, which is a minimum when the products are oriented perpendicular to the glide plane. Note that this relative positioning of the two $a\langle 010\rangle$ cores (i.e. the value of θ) is similar to that actually observed in the previous HRTEM studies (Mills and Miracle 1993).

For the edge orientation, if the products are aligned perpendicular to the glide plane, the anisotropic elasticity calculation gives a decomposition energy per unit length of $0{\cdot}79 \times 10^{-9}$ J m^{-1} (independent of separation). Although the radial force

vanishes, at finite temperatures the entropy will encourage the products to separate. Thus elasticity theory predicts the separation to occur in the manner observed by experiment; however, this is not the whole story. Because the decomposition energy is independent of distance and is roughly of the order of typical core energies, we must calculate the core energies to complete the analysis. To this end, atomistic calculations were performed on this system.

The statically minimized atomistic structure of a 'perfect' $a[011]$ edge dislocation is shown in fig. 7 (a). This atomic structure can be characterized by two extra (011) half-planes which are indicated in the figure as A and B. This structure is not decomposed or dissociated because both half-planes terminate at the same (011) plane, which would be the glide plane (GP) for the dislocation. The dislocation core is characterized by the octahedral unit indicated at the core of fig. 7 (a).

The 'perfect' dislocation core was found to transform into a distinctly different structure using molecular dynamics calculations (at a very low temperature) upon application of pure shear stresses relative to the nominal (011) glide plane. The structure shown in fig. 7 (b) was obtained after 10 ps having imposed a shear strain of 0·03 on the 'perfect' dislocation in fig. 7 (a) (the imposed strain is still present). This strain corresponds approximately to an initial applied shear stress of 940 MPa and would be present for deformation in the hard orientation. The core of fig. 7 (b) is no longer in the relatively planar configuration of fig. 7 (a) as can be seen by sighting along the (011) planes. In place of the open distorted octahedral unit which is characteristic of fig. 7 (a), two smaller tetrahedral units are formed, as indicated in fig. 7 (b). These units are the cores of individual $a[010]$ and $a[001]$ dislocations. This interpretation is supported by previous EAM calculations which have been conducted for isolated $a\langle 010\rangle$ dislocations (Farkas *et al.* 1991, Parthasarathy *et al.* 1993, Mills *et al.* 1993). Note that the two $a\langle 010\rangle$ cores in fig. 7 (b) have different atom types at their cores, being comprised of Ni and Al tetrahedra respectively. Thus these and other molecular dynamics calculations indicate a tendency for the perfect $a\langle 011\rangle$ core to decompose into narrowly separated $a\langle 010\rangle$ dislocations under the imposed shear strain. The same result is obtained if the applied shear strain is imposed in the opposite direction. Under no applied stress levels (exceeding 0·1 μ) was the 'perfect' $a\langle 011\rangle$ core observed to be glissile on its potential (011) glide plane.

Finally, in fig. 7 (c), we see what happens when we start with a configuration where the product $a\langle 010\rangle$ dislocations are positioned four (011) planes apart and then allow the system to relax. The products have not moved from their initial positions, which is not surprising given the lack of radial force from the elastic energy.

To compare the energies of the three configurations shown in fig. 7, we must adjust for differences in composition. If we define a cylinder surrounding the dislocation core, we can calculate the composition and energy of the included atoms. Two different atomistic configurations may differ slightly in composition and perhaps even total number of atoms, depending on how one draws the cylinder relative to the lattice. To compare the energies contained within the cylinder, one must compensate for the possible variation of composition. This is done by considering that the dislocation is in chemical equilibrium with the bulk material, which establishes a chemical potential for each species. The proper energy for comparison is then the total energy contained within the cylinder, relative to the same types of atoms in

Fig. 7

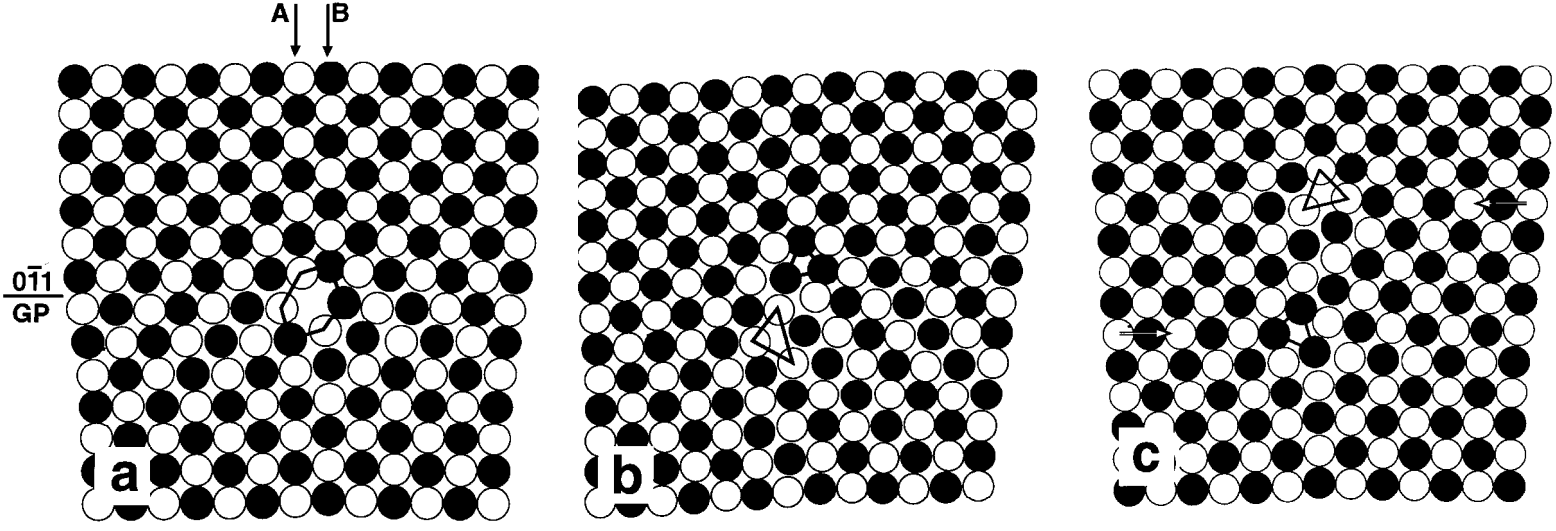

(*a*) (*b*) (*c*)

(*a*) Atomic arrangements near the core of a perfect $a[011]$ dislocation after relaxation using EAM. Note that, for this perfect dislocation, two extra (011) half-planes, which are indicated as A and B, terminate on the same (011) glide plane. Note the 'open' nature of the core which can be characterized by the octahedral unit as indicated. (*b*) Core structure formed during a molecular dynamics calculation performed at 0 K and an imposed shear strain of 0·03. The initial (unstrained) configuration was the perfect core shown in (*a*). Note that the core has transformed into the two triangular units indicated, which correspond to the locations of $a\langle 010\rangle$ dislocations in a nascent decomposed configuration. (*c*) Relaxed structure showing a more widely decomposed configuration. The arrows indicate discontinuous (011) planes.

the bulk. The total energy $E_T(R)$ of the dislocation within a cylinder of given radius R is then given by

$$E_T(R) = \sum_i E_i - \mu_{Ni} N_{Ni}(R) - \mu_{Al} N_{Al}(R), \quad (5)$$

where μ_{Ni} and μ_{Al} are the bulk chemical potentials for Ni and Al respectively, and the sum is over atoms within the cylindrical region. N_{Ni} and N_{Al} are the number of Ni and Al atoms within the cylindrical region, with the total number $N_T = N_{Ni} + N_{Al}$. The quantity E_i is described in the appendix; briefly, it is the energy per atom as calculated for the NiAl structure. The energy $E_T(R)$ is the energy by which different atomistic configurations can be compared. In general, the value of $E_T(R)$ should include contributions from firstly that part of the elastic strain energy contained within the cylinder, and secondly the core. The elastic strain energy includes both elastic self-energies as well as elastic interactions. Note that, with this procedure, only the elastic strain and interaction energies which lie within the computational cell are included. By this means, we can compare the *relative* energies of various configurations.

As can be seen from eqn. (2), a cylindrical region of radius R aligned along a straight dislocation contains an energy which depends linearly on ln R, with an offset determined by the core energy and the inner cut-off. This is also true for two dislocations (eqn. (3)), where the offset includes the angularly dependent term and the core energies of the individual dislocations. We shall thus plot the energy $E_T(R)$ against ln R. This is done in fig. 8 for the three configurations: perfect $a[011]$; nascent decomposition of $a[011]$ into two, closely spaced products; two products separated

Fig. 8

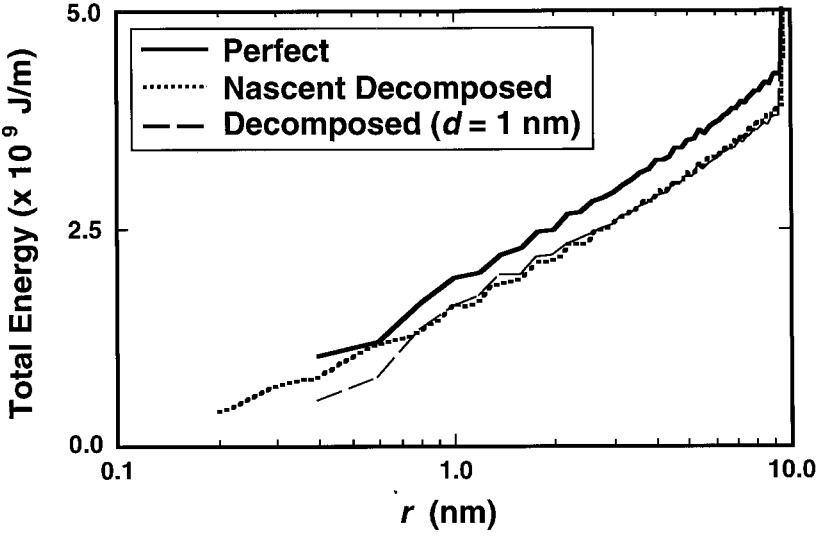

Total energy calculated using EAM as a function of radius within calculational cell for $a\langle 011\rangle$ dislocations in three configurations: perfect, nascent decomposed and more widely decomposed (separation distance, about 1 nm). Note the reduction in energy equal to about $0{\cdot}5 \times 10^{-9}$ J m^{-1} upon decomposition.

Energies of $a\langle 011\rangle$ dislocations for several configurations calculated using the EAM. Total energies (calculated using eqn. (5)) of relaxed structures within a 9 nm radius of the dislocation cores are indicated.

Dislocation configuration	Figure	Energy ($\times 10^9$ J m^{-1})
Perfect $a\langle 011\rangle$	7(*a*)	4·25
Perfect $a\langle 011\rangle$ (switched atom types)		4·26
Nascent decomposed $a\langle 011\rangle$	7(*b*)	3·80
Widely decomposed $a\langle 011\rangle$	7(*c*)	3·73

by five planes. The energy of the decomposed configuration of fig. 7 (*b*) was calculated after removing the imposed shear strain on the computational cell. (Note that the decomposed configuration remains even after removing the shear strain). For each configuration, we see clearly that the energy depends linearly on ln *R*, and that there is a constant offset among the three. The decomposed cores are seen to be lower in energy than the perfect dislocation. The calculated energy within a radius of 9 nm for the relaxed cores of fig. 5 is given in the table. The decrease in energy upon decomposition is about $0{\cdot}5 \times 10^{-9}$ J m^{-1}, somewhat less than the value predicted by anisotropic elasticity theory. The same results are also obtained if the atom types in the initial configuration are switched. The energy after switching the atom types is also provided in the table.

In summary, then, the elastic medium contributes $0{\cdot}79 \times 10^{-9}$ J m^{-1} to the decomposition energy. The atomistic calculations, which include changes both in the core and in the elastic medium, show the decomposition energy to be about $0{\cdot}5 \times 10^{-9}$ J m^{-1}. The difference would appear to be attributable to a change in the core energies which *disfavours* the reaction by about $0{\cdot}3 \times 10^{-9}$ J m^{-1} which is not enough to prohibit it. As noted above, in the elasticity theory the decomposition energy ΔW is *independent of system size* (i.e. *R*) for this decomposition case (see eqn. (4)). Thus, even though the atomistic calculation includes only that elastic strain energy within the computational cell, the elastic contribution to the decomposition energy should be completely included. The conclusion that the core energy actually disfavours decomposition implies that the two $a\langle 010\rangle$ cores are higher in energy than the single $a\langle 011\rangle$ core.

The mechanism of decomposition found in these calculations deserves additional comment. The nascent decomposed configuration is obtained by the formation and subsequent short-range glide of the two $a\langle 010\rangle$ dislocations on their respective {001} glide planes. This is a *conservative* process as demonstrated by the fact that it has been observed in the molecular dynamics calculations at 0 K. Once the short-range glide associated with decomposition takes place, additional motion of the decomposed core is not observed under this imposed shear stress since there is no glide force acting on the resultant $\langle 010\rangle$ dislocations. This particular decomposition process is only possible for an $a[011]$ dislocation of edge character since its [100] line direction is common in *both* (001) and (010) glide planes of the product $a\langle 010\rangle$ dislocations. As the line orientation deviates from [100], these low-index glide planes are not available to initiate the decomposition process.

Thus far, we have dealt with the mechanism by which the perfect $a[011]$ dislocation may transform into the nascent decomposed core. The TEM evidence clearly indicates, however, that a wide range of decomposition distances can arise, and that

climb is an important component of this continued decomposition process. For an axial stress in the hard orientation, one of the product $a\langle 010\rangle$ dislocations will experience a climb force. This situation is illustrated in fig. 9. In the process of climbing in response to the applied stress, vacancies will either be produced or absorbed (they will be absorbed by dislocation A shown in fig. 9). The vacancies required for climb to occur may originate far from the dislocations, or they may be produced by the coordinated climb of the companion $a\langle 010\rangle$ dislocation (labelled B) as shown in the figure. This latter possibility is particularly likely since not only are the dislocations in close proximity, but also they are actually linked together by the non-edge portion of the $a[011]$ dislocation, which appears to be relatively compact as described in § 3. Consequently, the coordinated climb of the product $a\langle 010\rangle$ dislocations could occur by the transfer of vacancies from one $a\langle 010\rangle$ dislocation to the other via pipe diffusion. This possibility could explain the experimental evidence for extensive climb of dislocations at quite low homologous temperatures, as was described in the previous section. In the course of decomposing by this climb process, glide of the individual $a\langle 010\rangle$ dislocations on their corresponding {001} planes could also occur in order to minimize the elastic interaction between the $a\langle 010\rangle$ dislocations or in response to other internal stresses. These considerations can therefore qualitatively explain the operation of both climb and glide during continued decomposition of the near edge segments of the $a[011]$ dislocations.

Fig. 9

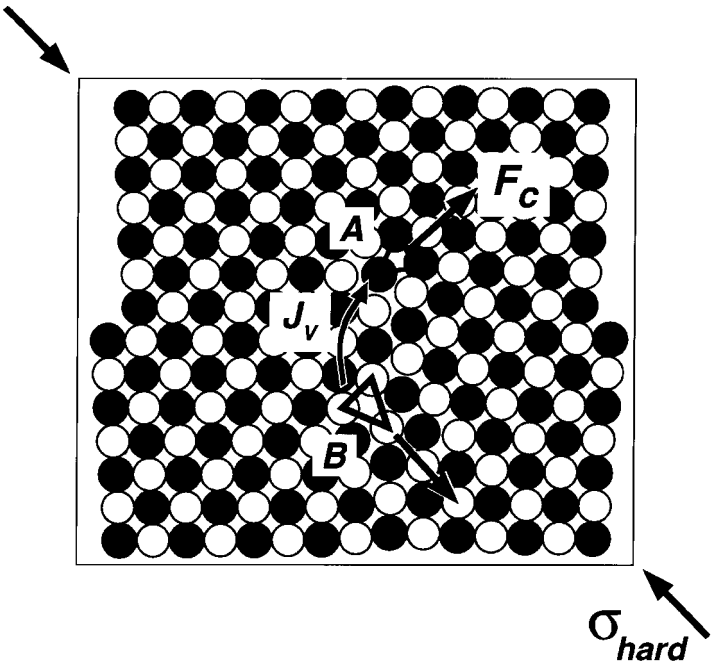

Atomic-level picture of climb of $a\langle 010\rangle$ dislocations for decomposed $a[011]$ edge dislocation under action of external stress in the [001] 'hard' orientation. A climb force F_c exists for dislocation A, while the cooperative climb of both A and B can occur by transfer of vacancies in the direction illustrated.

§ 5. Basis of dislocation model

The results of both the experimental and the theoretical work described above indicate that the edge segments of $a\langle 011\rangle$ dislocations undergo a core transformation which renders these dislocations unable to glide on their slip planes. However, under an axial stress in a $\langle 001\rangle$ direction, a climb force is operative on one of the decomposed dislocations. Climb of both $a\langle 010\rangle$ dislocations in the decomposed segments can occur by a cooperative diffusion-controlled process in which vacancies are transferred from one 'arm' of the decomposed configuration to the other. In this cooperative process, the long-range diffusion of vacancies is not required. Furthermore, the vacancy transfer can occur relatively rapidly (and at a lower temperature) along the cores of the $a\langle 010\rangle$ dislocations, rather than through the lattice.

Given this scenario for the decomposition of the edge segments, the question remains as to how overall motion of the $a\langle 011\rangle$ dislocations occurs? In spite of the apparent immobility of the edge segments, the dislocation microstructure seen in fig. 1 suggests that $a\langle 011\rangle$ loops do expand outwards under the applied stress, with the non-edge segments apparently being far more mobile. The following model for the motion of a near-edge segment of an $a\langle 011\rangle$ dislocation is offered as a possibility for the rate-controlling process within this deformation regime. The qualitative aspects of this model have been introduced previously (Mills *et al.* 1995b). Here we develop an expression for the strain rate which we then compare with the observed behaviour of hard-oriented NiAl.

The model is based on the assumption that the propagation of near-edge segments may occur by the *lateral* motion of macrokinks, such as those identified in fig. 1. As shown schematically in fig. 10, the model envisages that the lateral motion of screw-character macrokinks is constrained by the decomposed edge segments which must be constricted. This constriction requires both glide and climb of the decomposed sections. An important feature of the model is that the climb component of this constriction process can occur by *pipe* diffusion from one $a\langle 010\rangle$ dislocation to the other. In the simplified development of the present model, the following assumptions are made.

(*a*) The elastic interaction between dislocations is ignored.
(*b*) Line tension along the $a\langle 010\rangle$ dislocations of the decomposed segments is ignored.
(*c*) The frictional force for the motion of the macrokink is assumed to be negligible.
(*d*) Decomposition occurs entirely by climb so that the $a\langle 010\rangle$ dislocations are in the form of prismatic half-loops (as illustrated in fig. 10).
(*e*) A periodic array of identical macrokinks is assumed to be arranged along the skewed $a\langle 011\rangle$ dislocation line.

The change in energy upon advancing the macrokink a distance $\mathrm{d}l$ is given by

$$\mathrm{d}W = (-\tau b^{011} h + \sigma b^{001} d + W^{011}_{\mathrm{self}} - 2W^{001}_{\mathrm{self}})\,\mathrm{d}l, \qquad (6)$$

where σ is the applied stress in the hard $[001]$ orientation, τ is the resolved shear stress for the $a[011]$ dislocation on the (011) plane, h is the height of the macrokink and d is the distance over which the $\langle 010\rangle$ dislocations have decomposed out of the (011) glide plane. The second term of eqn. (6) is the work required to move the $a[001]$ prismatic half-loop, the motion of which is opposed by the applied stress. There is no

Fig. 10

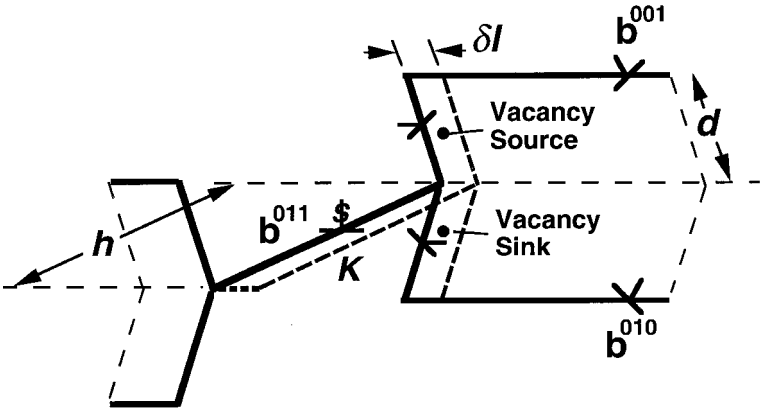

Geometry near a macrokink K on an $a[011]$ edge dislocation used in the formulation of the deformation model described in the text. The $a[011]$ segments of edge orientation are assumed to be decomposed by climb into $a[010]$ and $a[001]$ dislocations. Glide of the $a[011]$ macrokink on its (011) glide plane by a distance δl requires constriction of the decomposed segment via short-circuit vacancy transfer from the $a[001]$ to the $a[010]$ dislocation. At the other end of the macrokink, a segment of perfect $a[011]$ dislocation of length δl is created along edge orientation for a macrokink advance of δl. The macrokink height h and decomposition distance d are indicated.

applied force on the $a[010]$ prismatic half-loop. The edge segment deposited by the moving macrokink is assumed to be an undecomposed $a[011]$ segment of length $\mathrm{d}l$.

During motion of the macrokink to the right as sketched in fig. 10, vacancies must be transferred from the $a[001]$ dislocation (the vacancy 'source') to the $a[010]$ dislocation (the vacancy 'sink'). The macrokink can advance by a distance of about $a_0/2$ (where a_0 is the lattice parameter) if a column of atoms is transferred from the vacancy 'sink' to the vacancy 'source'. Therefore the number of vacancies transferred for a general advancement $\mathrm{d}l$ is

$$\mathrm{d}n = \frac{d}{a_0^2}\,\mathrm{d}l. \tag{7}$$

The elastic energy released per vacancy transferred is given by

$$w = -\frac{\mathrm{d}W}{\mathrm{d}l}\frac{\mathrm{d}l}{\mathrm{d}n}. \tag{8}$$

Since $W_{\mathrm{self}}^{011} = 2W_{\mathrm{self}}^{010}$ (U. Glatzel 1992, unpublished work), then

$$w = (\tau b^{011} h - \sigma b^{001} d)\frac{a_0^2}{d}. \tag{9}$$

The vacancy supersaturation at the source (the $a[001]$ dislocation) is

$$\Delta c = c^0\left[\exp\left(\frac{w}{kT}\right) - 1\right], \tag{10}$$

where c^0 is the equilibrium vacancy concentration. Using the limit in which $\Delta c \ll c^0$, we may write

$$\Delta c \approx \frac{c^0 w}{kT}. \tag{11}$$

Fig. 11

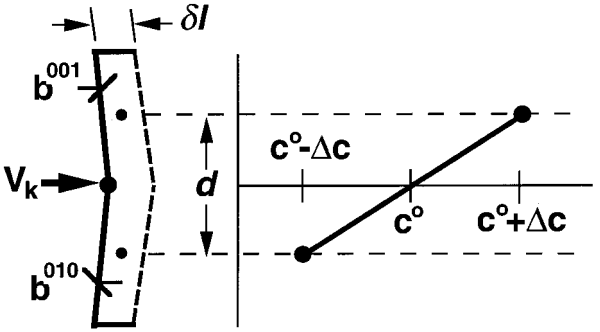

Vacancy concentration profile assumed in the model. The vacancy source and sink ($a[001]$ and $a[010]$ prismatic loops respectively) are taken as 'points'. Vacancy transfer occurs by pipe diffusion and is conservative so that the midpoint of the concentration profile is equal to the equilibrium vacancy concentrations c^0.

With this expression for the vacancy supersaturation at the source, we can consider the steady-state solution for this diffusion problem as illustrated in fig. 11. Here, we represent the vacancy source and sink as 'point' sources which are separated by the decomposition distance d. Since the transfer of vacancies is assumed to be conservative, with no net gain or loss of vacancies to the local system, then the equilibrium vacancy concentration c^0 should exist in between the 'point' source and sink. For this simple model, the vacancy flux can easily be calculated as

$$J = -D_V \frac{dc}{dx} = \frac{D_S}{\Omega c^0} \frac{2\Delta c}{d}, \tag{12}$$

where Ω is the atomic volume, and D_V and D_S are the vacancy and atomic self-diffusion coefficients respectively. We further assume that the conservative transfer of vacancies occurs by the easiest possible path, via diffusion along the cores of the $a\langle 010\rangle$ prismatic loops. Therefore the relevant diffusion coefficient is that for pipe diffusion, namely D_{pipe}. Combining eqns. (9), (11) and (12), the vacancy flux may be written as

$$J = \frac{2a_0^2 D_{pipe}(\tau b^{011} h - \sigma b^{001} d)}{\Omega d^2 kT}. \tag{13}$$

The current of atoms along the dislocation 'pipe' is approximated as Ja_0^2, where a_0^2 is the assumed cross-sectional area of the 'pipe'. The macrokink velocity can then be obtained from

$$V_k = Ja_0^2 \frac{dl}{dn} \tag{14}$$

or

$$V_k = \frac{4a_0^3 D_{pipe}(\tau b^{011} h - \sigma b^{001} d)}{d^3 kT}. \tag{15}$$

where Ω is taken as $a_0^3/2$. For deformation in the hard orientation, $\tau = \sigma/2$ and with

$b^{011} = 2^{1/2}b^{001}$ we arrive at a final form for the macrokink velocity as

$$V_k = \frac{4a_0^4 D_{pipe}\sigma(h/2^{1/2} - d)}{d^3 kT} \quad (16)$$

Thus the velocity of the macrokinks will depend on temperature (through D_{pipe}/T), applied stress, decomposition distance d and macrokink height h. The variation in the macrokink velocity with the latter two geometrical parameters is shown in fig. 12. In this plot, the activation energy for pipe diffusion (150 kJ mol^{-1}) is simply taken as half that for lattice self-diffusion, and the value of $D_S = 4{\cdot}4 \times 10^{-4}$ m^{-2} s^{-1} is taken from the data of Hancock and McDonnell (1971). The stress (500 MPa) and temperature (873 K) are reasonable values based on experimental constant-strain-rate tests performed by Kim and Gibala (1991) for a Ni–47·5% Al–0·6% Si–0·08% Fe alloy in which $a\langle 011\rangle$ activity has been clearly identified. The macrokink velocity increases quite rapidly with decreasing d since this parameter determines not only how many vacancies must be transferred for a given macrokink advance but also the path length for diffusion. The value of h is important since this parameter effectively determines the force which the macrokink can exert to constrict the decomposed segment.

From the present diffraction contrast TEM observations, we roughly approximate an 'average' value of d of about 3 nm. Correlating the small deviations in the edge line direction, such as those indicated in fig. 1, with the macrokinks, a reasonable value for h is about 50 nm. From fig. 12, this combination of parameters yields a macrokink velocity of about $2{\cdot}5 \times 10^{-4}$ ms^{-1}. To determine whether this velocity is reasonable in terms of the overall strain rate which could be produced by such a

Fig. 12

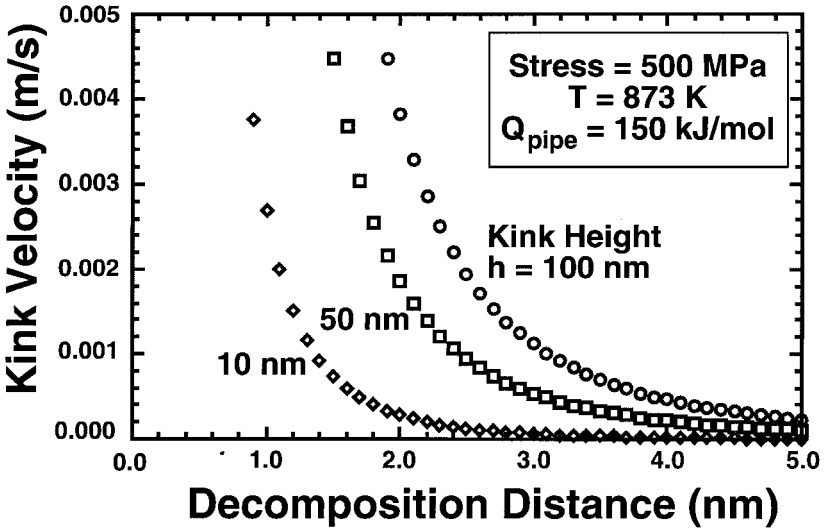

Variation in macrokink velocity with both decomposition distance d and macrokink height h calculated using eqn. (16). Calculations for an axial stress of 500 MPa and a temperature of 873 K and assuming an activation energy of 150 kJ mol^{-1}, which is approximately half the value for lattice self-diffusion.

process, we may approximate the shear strain rate using

$$\dot{\gamma} = N_k b V_k, \tag{17}$$

where N_k is the density of macrokinks. The value of N_k can be related to the total dislocation density N_T using

$$N_k = \frac{l_k}{l_T} N_T, \tag{18}$$

where l_T and l_k are the total line length and macrokink line length respectively. Approximating the value of $l_k / l_T = \frac{1}{50}$, based once again on the observed dislocation structures, the predicted shear strain rate is about $1 \times 10^{-3}\,s^{-1}$. This strain rate is in remarkably good agreement with the imposed strain rate experienced by the sample. The assumptions and approximations required to formulate the present model clearly make this quantitative agreement somewhat fortuitous. Nevertheless, this model of a pipe-diffusion-mediated glide process does seem to produce a kinetic law which is reasonable. In comparison, if this process were instead mediated by lattice diffusion, and accounting for a larger possible cross-sectional area for diffusion of d^2, the shear strain rate under the same conditions would be $1{\cdot}2 \times 10^{-10}\,s^{-1}$, many orders of magnitude too slow to account for the experimental results.

§ 6. Discussion

The diffusion-mediated glide mechanism proposed here would clearly imply that dislocation motion should be thermally activated and can explain several important aspects of deformation in the hard orientation. Firstly the inactivity of $a\langle 011\rangle$ dislocations at low temperatures can be rationalized since the formation of the sessile decomposed edge components will cause blocking of $a\langle 011\rangle$ sources. Secondly at higher temperatures (above the BDTT), the yield strength should decrease dramatically with increasing temperature as the motion of non-edge components becomes easier. Such a mechanism also implies a mobility-controlled deformation process which is consistent with the observation of yield points in constant-strain-rate tests (Field *et al.* 1991) and sigmoidal primary creep transients at elevated temperatures (Forbes *et al.* 1993).

The relatively weak (linear) dependence of the dislocation velocity on stress would suggest that the flow stress should vary strongly with imposed strain rate. While a systematic examination of the strain-rate dependence of hard-oriented NiAl has not been performed, there are indications that both the yield strength and the BDTT increase significantly with strain rate (Field *et al.* 1991, Miracle 1993, Noebe *et al.* 1993). The predicted dependence of flow stress on strain rate is at best qualitative here since we have not attempted to specify the dependence of structure (i.e. the dislocation density and the characteristic structural parameters d and h) on stress. Perhaps more directly relevant are strain-rate sensitivity (SRS) measurements in which the change in flow stress is measured upon a jump in strain rate. If we assume that the 'structure' remains constant during the strain-rate jump, then the stress dependence of the dislocation velocity can be deduced. Such experiments have been conducted by Pascoe and Newey (1971) on stoichiometric hard-oriented NiAl. For strain-rate changes between $1{\cdot}2 \times 10^{-3}$ and $1{\cdot}2 \times 10^{-4}\,s^{-1}$, they reported values of SRS (i.e. $d\tau / d(\ln \dot{\gamma})$) which vary from about 70 MPa at 650 K to about 30 MPa at 800 K. For the conditions described above ($\tau = 250$ MPa and $T = 873$ K) and a similar strain-rate change, the predicted values of SRS with the present model is about 97 MPa.

As mentioned above, in this simple model the evolution laws for the dislocation density and dislocation structure have not been prescribed. In addition, the characterization of the dislocation structure with fixed values of d and h is clearly a gross approximation since a *distribution* of these parameters is clearly a feature of the observed microstructure, as described above. As a consequence of these oversimplifications, the model cannot explicitly predict the variation in the flow stress and dislocation structure with strain. For example, consider a case in which a decomposed segment of the $a\langle 011\rangle$ dislocation is *not* 'zipped' back together by the motion of a macrokink. This might occur for example if the nearby macrokinks are of insufficient length to apply the required force for motion. Since a climb force will *always* exist on one of the product $a\langle 010\rangle$ segments, then the decomposition distance (d in fig. 10) will tend to increase continuously with time under load. As d increases, it becomes ever more difficult for even a large macrokink to constrict the decomposed segment. Thus there should be a general tendency for $a\langle 011\rangle$ dislocations to decompose by climb into $a\langle 010\rangle$ dislocations as a function of strain. More complete decomposition will also be favoured if there is a deviation from an axial stress in the hard orientation, since under these conditions there will exist a resolved shear stress for the *glide* of the product $a\langle 010\rangle$ dislocations on their respective {001} glide planes. Such a situation could occur simply owing to misalignment of the test sample from the hard orientation. Rotation of the sample away from the hard orientation *during* deformation could also give rise to this situation.

Thus consideration of the possible strain dependence of decomposition by both climb and glide would suggest that deformation dominated by $a\langle 011\rangle$ dislocations may be limited to relatively small strains. At larger strains, it is expected that the microstructure may be dominated by the $a\langle 010\rangle$ decomposition products. While there has been no systematic study of the strain dependence of the dislocation microstructure in NiAl, Kim and Gibala (1991) have found that nearly *all* the dislocations present in a Ni-47·4% Al-0·6%Si-0·08% Fe alloy were of the $a\langle 011\rangle$ type after a strain of 2·6% at 873 K in the hard orientation. Kim and Gibala (1991) further noted that, at larger strains (10%), the density of $a\langle 011\rangle$ dislocation declined dramatically in preference to $a\langle 010\rangle$ dislocations.

While the results of the model presented above are encouraging, this derivation is only approximate and requires significant improvement. In particular, the elastic interaction between the decomposed $a\langle 010\rangle$ dislocations is not at present considered in this development, nor is the actual shape of the dislocation arrangements which determines the diffusion path length. Ultimately, a dynamical simulation in which the process of climb decomposition is allowed to be competitive with the diffusion-mediated glide process described here will be required to model more accurately the strain dependence of the dislocation structure and kinetics.

§ 7. Conclusions

TEM studies have revealed that $a\langle 011\rangle$ edge dislocations in NiAl tend to decompose into two separate $a\langle 010\rangle$ edge dislocations with orthogonal Burgers vectors. A variety of decomposition distances have been observed, from approximately 1 nm to over 100 nm. Based on tilting experiments for the more widely decomposed segments, decomposition occurs through a combination of both climb and glide. The decomposition tends to inhibit the motion of $a\langle 011\rangle$ dislocations, as evidenced by the observed elongation of the loops along edge orientation. These observations are consistent with EAM calculations which indicate that a perfect $a\langle 011\rangle$ edge disloca-

tion is indeed a metastable configuration. Molecular dynamics EAM calculations have shown that upon the application of shear stresses a nascent decomposed structure is formed owing to the short-range glide of the product $a\langle 010\rangle$ dislocations. Decomposition occurs in preference to glide of the perfect $a\langle 011\rangle$ dislocation and is favoured along the edge orientation based on both anisotropic elasticity and EAM calculations. The core energy is found to increase slightly upon decomposition, since a single $a\langle 011\rangle$ core converts into two $a\langle 010\rangle$ cores. However, the energy decrease due to the elastic interaction between $a\langle 010\rangle$ dislocations makes decomposition energetically favourable. A variety of distances separating the two $a\langle 010\rangle$ dislocations may subsequently arise owing to a combination of coordinated climb and glide of the $a\langle 010\rangle$ dislocations. The decomposition of $a\langle 011\rangle$ dislocations effectively locks the edge portions of these dislocations, suggesting that motion of these dislocations is instead controlled by the lateral movement of non-edge segments ('macrokinks'). A simple dislocation model has been developed on the premise that the motion of non-edge macrokinks requires the constriction of the decomposed edge segments. In the model, it is assumed that this constriction process will involve the transfer of vacancies from one $a\langle 010\rangle$ dislocation to the other via pipe diffusion. The postulated diffusion-mediated glide model for the $a\langle 011\rangle$ dislocation appears to be in reasonable agreement with the observed kinetics of deformation, as well as the strong temperature and strain-rate dependences found in NiAl at intermediate temperatures.

Acknowledgements

The authors would like to acknowledge D. B. Miracle for inspiring this work and providing the NiAl bicrystal specimens, S. M. Foiles for his assistance in modifying the EAM functions used in this work, J. E. Angelo for contributions to the image analysis and U, Glatzel for making available his code for performing anisotropic elastic calculations. Many helpful discussions with W. D. Nix, K. R. Forbes, R. D. Noebe, H. L. Fraser and S. A. Dregia are also gratefully acknowledged. Support for this work was provided in part by the US Department of Energy, Office of Basic Energy Sciences under contract No. DE-AC04-94AL85000 as well as contract No. DE-FG-02-96ER45550 (for M.J.M. and S.R.), as well as the National Science Foundation under grant No. 95-10259 (for M.S.D.).

APPENDIX

To compare the energies of the different atomistic configurations which contain different total numbers of atoms or different compositions, we must establish a reference, which we take to be perfect bulk material, thus establishing a chemical potential for each species in the calculation. The proper energy for comparison is then the atomistic energy *relative to* the atomistic energy of the same atoms in the perfect bulk, which is just the sum of chemical potentials of the constituent species. Thus, $G = E - \sum_i \mu_i$ is the proper quantity for comparison.

Within the EAM, the energy is computed as a sum over all atoms: $E = \sum_i E_i$, where the 'atomic energies' are given by $E_i = F_i\left[\sum_{j\neq i} \rho_j(R_{ij})\right] + \frac{1}{2}\sum_{j\neq i} \varphi_{ij}(R_{ij})$. It is important to stress that the quantities E_i are *completely arbitrary*; the only physical quantity in the EAM is the total energy; how that energy is divided is arbitrary and any quantity which depends on that division is not physical. Connected with this ambiguity is a simple linear transformation which changes E_i arbitrarily but

preserves the total energy: $F_i(\rho) \to F_i(\rho) + \alpha_i\rho$ and $\varphi_{ij}(R) \to \varphi_{ij}(R) - \alpha_i\rho_j(R) - \alpha_j\rho_i(R)$, where the α_i are arbitrary numbers.

However, we can attach physical significance to the E_i if we require that, for a perfect bulk crystal, they equal the chemical potentials μ_i. This requirement eliminates any ambiguity in the quantity (by fixing the values of the α_i) and makes evaluation of the quantity G quite straightforward.

References

Ball, A., and Smallman, R. E., 1966, *Acta metall.*, **14**, 1517.

Daw, M. S., and Baskes, M. I., 1984, *Phys. Rev.* B, **29**, 6443.

Farkas, D., Pasianot, R., Savino, E. J., and Miracle, D. B., 1991, *High-Temperature Ordered Intermetallic Alloys IV,* Materials Research Society Symposium Proceedings, Vol. 213 (Pittsburgh, Pennsylvania: Materials Research Society) p. 223.

Field, R. D., Lahrman, D. F., and Darolia, R., 1991, *Acta metall. mater.*, **39**, 2951.

Foiles, S. M., and Daws, M. S., 1987, *J. Mater. Res.*, **2**, 5.

Forbes, K. R., Glatzel, U., Darolia, R., and Nix, W. D., 1993, *High-Temperature Ordered Intermetallic Alloys V,* Materials Research Society Symposium Proceedings, Vol. 288 (Pittsburgh, Pennsylvania: Materials Research Society) p. 45.

Fraser, H. L., Smallman, R. E., and Loretto, M. H., 1973a, *Phil. Mag*, **28**, 651.

Fraser, H. L., Loretto, M. H., and Smallman, R. E., 1973b, *Phil. Mag*, **28**, 667.

Glatzel, U., Forbes, K. R., and Nix, W. D., 1993, *Phil. Mag.* A, **67**, 307.

Hancock, G. F., and McDonnell, B. R., 1971, *Phys. Stat. sol.* (a), **4**, 143.

Hirth, J. P., and Lothe, J., 1982, *Theory of Dislocations* (New York: Wiley).

Kim, J. T., 1990, Ph.D. Dissertation, University of Michigan.

Kim, J. P., and Gibala, R., 1991, *High-Temperature Ordered Intermetallic Alloys IV,* Materials Research Society Symposium Proceedings, Vol. 213 (Pittsburgh, Pennsylvania: Materials Research Society) p. 261.

Lahrman, D. F., Field, R. D., and Darolia, R., 1991, *High-Temperature Ordered Intermetallic Alloys IV,* Materials Research Society Symposium Proceedings, Vol. 213 (Pittsburgh, Pennsylvania: Materials Research Society) p. 603.

Loretto, M. H., and Wasilewski, R. J., 1971, *Phil. Mag,* **23**, 111.

Mills, M. J., Angelo, J. E., Daw, M. S., Weinburg, J. D., and Miracle, D. B., 1995a, *Mater. Sci. Eng.*, **A192–A193**, 134.

Mills, M. J., Daw, M. S., Angelo, J. E., and Miracle, D. B., 1995b, *High-Temperature Ordered Intermetallic Alloys VI,* Materials Research Society Symposium Proceedings, Vol. 364 (Pittsburgh, Pennsylvania: Materials Research Society) p. 401.

Mills, M. J., Daw, M. S., Foiles, S. M., and Miracle, D. B., 1993, *High-Temperature Ordered Intermetallic Alloys V,* Materials Research Society Symposium Proceedings, Vol. 288 (Pittsburgh, Pennsylvania: Materials Research Society) p. 257.

Mills, M. J., and Miracle, D. B., 1993, *Acta metall. mater.*, **41**, 85.

Miracle, D. B., 1990, Ph.D. Dissertation, The Ohio State University; 1991, *Acta metall. mater.*, **39**, 1457; 1993, *ibid.* **41**, 649.

Noebe, R. D., Bowman, R. R., and Nathal, M. V., 1993, *Int. Mater. Rev.*, **38**, 193.

Parthasarathy, T. A., Rao, S. I., and Dimiduk, D. M., 1993, *Phil. Mag.* A, **67**, 643.

Pascoe, R. T., and Newey, C. W. A., 1968, *Phys. Stat. sol.,* **29**, 357; 1971, *Metall. Sci. J.*, **5**, 50.

Rao, S. I., Woodward, C., Parthasarathy, T. A., and Dimiduk, D. M., 1991, *High-Temperature Ordered Intermetallic Alloys IV,* Materials Research Society Symposium Proceedings, Vol. 213 (Pittsburgh, Pennsylvania: Materials Research Society) p. 125.

Rusovic, N., and Warlimont, H., 1977, *Phys. Stat. sol.* (a), **44**, 609.

Wasilewski, R. J., Butler, S. R., and Hanlon, J. E., 1967, *Trans. AIME*, **239**, 1357.

Yoshida, M., and Takasugi, T., 1991, *High-Temperature Ordered Intermetallic Alloys IV,* Materials Research Society Symposium Proceedings, Vol. 213 (Pittsburgh, Pennsylvania: Materials Research Society) p. 273.